How to Cite:
Hazela, B., Aarti, Khandelwal, A., Soundararajan, S., Vyas, R., & Balaji, A. (2022). Biomedical image restoration using machine learning GPU acceleration approach for precision improvement. *International Journal of Health Sciences*, *6*(S3), 1919–1933. https://doi.org/10.53730/ijhs.v6nS3.5892

Biomedical image restoration using machine learning GPU acceleration approach for precision improvement

Bramah Hazela
Assistant Professor, Department of Computer Science and Engineering, Amity School of Engineering and Technology, Amity University, Lucknow Campus, Lucknow – 226010

Aarti
Assistant Professor, Computer Science and Information Technology, Central University of Haryana, Jant-Pali, Mahendergarh, Haryana, India, 123031

Arika Khandelwal
Associate Professor, Department of Computer Science and Engineering, G.H.Raisoni College of engineering, Nagpur, Maharashtra – 440016

Soundararajan S.
Professor, Department of Computer Science and Engineering, Velammal Institute of Technology, Chennai – 601204

Ruchi Vyas
Assistant Professor, Department of Computer Science and Engineering, Geetanjali Institute of Technical studies, Udaipur, Rajasthan, India

A. Balaji
Associate Professor, Department of Computer Science and Engineering, Guntur engineering college, Yanamadala, Andhra Pradesh 522019

***Abstract*---**Focusing the image in a single x-ray projection, an algorithm proposed for actual time volumetric image rebuilt and 3-dimensional location of the lump. Using the Principal Component Analysis (PCA) initialize the parameterized Deformation Vector Fields (DVF) of pulmonary movement. By adjusting the PCA coefficients, applied the DVF applied to optimize the reference image so that, the simulated projection of the rebuilt image matches the observed projection. The digital phantom & patient information was used to evaluate the technique. The phantom has an average relative image rebuilt error of 7.5 percent and a 3-dimensional location of the lump

International Journal of Health Sciences ISSN 2550-6978 E-ISSN 2550-696X © 2022.
***Corresponding author**: Hazela, B.*
Manuscript submitted: 18 Nov 2021, Manuscript revised: 09 Feb 2022, Accepted for publication: 27 March 2022

inaccuracy of 0.9 mm, correspondingly. The patient's location of the lump inaccuracy is less than 2 mm. On a GPU NVIDIA C1060, recreating a single volumetric image from every projection takes about 0.2 & 0.3 secs for patient and phantom. From a single image, clinical relevance could lead to reliable 3-dimensional lump tracking.

***Keywords*---**image rebuilt, location of the lump, pulmonary movement, gpu, pulmonary carcinoma, radiation therapy.

Introduction

Lump movement control is a difficult and critical issue in current highly conformal pulmonary carcinoma radiation therapy [1]. Poor lump movement management can result in an inadequate method that provides and an unduly high dosage in normal tissues [2]. As a result, precise information on actual time lump movement, mobility during therapy administration is critical for pulmonary carcinoma radiation success. [3]. [4] Used a general B-spline movement model to predict 3D breathing, movement projections on cone beam. Forever, because the system has a large number of parameters, several projections across a wide range of directions must be utilized. As a result, the estimation method is retrospective rather than the actual time. The purpose of this study is to show that pulmonary movement data can be extracted in actual time from one x-ray projection [5]. This is accomplished by making efficient, utilize the preceding data provided by 4DCT / 4DCBCT, which PCA effectively represents the distortion of the entire pulmonary at various periods. The PCA pulmonary movement model's intrinsic regularization allows us to obtain the volumetric image of the patient from one projection [6]. The technique is designed on a graphics processing unit for actual-time efficiency.

Far as we understand, 2 spatiotemporal systems do not imply regular respiratory rate and are hence better suited to describing respiratory movement in unconstrained breathing settings. [7] Developed a 5D pulmonary movement model that permits characterization of hysteresis & the irregular respiration rate and is parameterized by vital capacity and airflow recorded with spirometry. A huge amount of patients was recently evaluated in the system. In general, a voxel's position is calculated by superimposing 2 displacement vectors caused by vital capacity and airflow over the top of its reference position at 0 vital capacity & airflow. In the system, there are 5 independent variables. Vital capacity, airflow, and the 3-dimensional reference position are the five variables [8].

Materials and Methods

In a 4-Dimensional Computerized Tomography (4DCT) set of data, [9] performed PCA on the 3-dimensional distortion field produced from a deformable image registration of both reference phases & other phases. In 4DCT of 4 patients, they discovered that 2 main constituents are sufficient to adequately represent respiratory movement. It is necessary to provide some clarity on the term PCA pulmonary movement modeling. Only the Eigen decomposition of pulmonary

movement information is referred to as PCA pulmonary movement modeling as in the following [10]. Any subsequent information processing is not included in the 'PCA pulmonary movement modeling,' and could be applied specifically. Even though the PCA movement model described by [11] appears promising based on the findings of a limited group of patients, more research is needed to determine why it operates and whether there is a deeper relationship between the 2 pulmonary movement models than their surface mathematical similarities. Low's 5D pulmonary movement model is a physiological concept that is based on pulmonary architecture and movement dynamics [12]. The PCA movement model, on either side, is more mathematically flavored and is based on a multivariate statistical technique.

A primary purpose of this study should not be to compare the two previously described pulmonary movement systems. Rather, we want to learn more about the efficiency of PCA in modeling the intricate spatiotemporal interactions that characterize the overall pulmonary movement. With such a model, we may operate the pulmonary movement model and thereby derive the lump movement utilizing the sparse subset of the pulmonary, such as an implanted flag [13], the diaphragm, or its chest area. From this standpoint, the goal and scope of this study differ from and is far broader than of [14]. The following are the primary contributions to this work, and what sets it apart from past work. Initially, we propose a theoretical methodology for a thorough examination of the Principal Components Analysis-based pulmonary movement model. The theoretical explanation for Principal Components Analysis's success in modeling pulmonary movement is presented [15]. We'll see that it's closely related to Lows physiological 5D pulmonary movement model, and these 2 models are truly equal in certain situations [16].

The selection of 2 principal components in [17] is rather heuristic and is dependent on measurements of an eigenvalue. We tried to explain the important question about how many principal components are required to model pulmonary movement in a statistical model in this paper. A difference from earlier research is how the PCA movement model is utilized to predict pulmonary movement once it is built. To forecast pulmonary movement, the present diaphragm location and its past value are employed as surrogates in [18]. In this paper, we will present an alternate method for predicting pulmonary movement utilizing the PCA model, and illustrates the feasibility of deriving the whole pulmonary movement from the single fiducial marker measurement.

As a predictor-corrector technique, we used the algebraic restoration technique OS-SIRT. SIRT & SART are the 2 extremes in this system, includes SIRT being just one subgroup & SART having M [19]. While there is no variation in the runtime of each repetition on the Central processing unit, due to the frequent projection back-projection context changes that disrupt parallelism & flow of data on the GPU, a repetition using SART is generally the slowest. This has important consequences for the total reconstructive wall clock time, as SART is no more the quickest technique in the free of noise scenario [20]. Other researchers have noticed this impact [21-22], but their focus was exclusively on reconstructing speed. In comparison, we discovered in our study that when reconstructions

quality is taken into account, these correlations change, and SART is becoming more efficient once more.

Enforcing positivity is a basic regularization method. As additional regularization, the approach of the total variation was introduced in [23]. TV reduction (TVM) flattens the density profile in local areas, which makes it ideal for reducing the noise & streak artifacts. The technique has been proven to function effectively in diverse defective imaging scenarios predicated on the premise of a relatively sparse gradient subject, although this premise may not be practical in practice. The ROF type and the TV-L 1 model are 2 well-known TV models that are commonly employed in machine vision [24]. As the mitigation technique of the models' power functional, a variety of variational methods have been developed. They are mostly dependent on using an optimization algorithm to overcome the related Euler Lagrange simultaneous equations [25]. These techniques are ideal for removing noise & other undesirable tiny scale features while keeping edges intact.

Methodology

The core idea behind our research is to first create a pulmonary movement model using a few PCA coefficients, and then alter the deformation vector field applied to a reference Computed tomography to match the x-ray projection images recorded during treatment. Whenever they reference Computed tomography or 4DCT in the following, the same idea can be applied to 4DCBCT or CBCT. The principal Component is used to parameterize pulmonary movement in our technique. [19] Proposed the PCA pulmonary movement model, which was recently proved in [20] to have a tight theoretical relationship with the physiological 5D pulmonary movement model [21]. Pulmonary movement, expressed as a vector function $V(f)$, could be represented in the PCA model a linear combination of an eigenvector according to the biggest eigenvector:

$$V(f) \approx \bar{V} + \sum_{i=1}^{I} X_i Y_i(f) \qquad (1)$$

These are the principal components derived through PCA and are solely spatial variables. The real numbers work (f) is PCA values which are just time-dependent. It is really important to note that such principal components were stable following Principal Component Analysis, and the variation pulmonary movement is controlled by the development of the PCA values. The PCA pulmonary movement structure is suitable for our project for two primary reasons. Firstly, in terms of the smallest average, PCA offers the best straight description of the information. Secondly, the PCA movement figure's depiction is subject to inherent regularization.

$$\|\Delta X\|^2 \leq \sum_i \left(1/\sigma^2\right) . \|\Delta V\|^2 \qquad (2)$$

The principal components from the PCA can be used to illustrate these. That implies because if two meshes shift in the same way, PCA will reflect their movement in the same way [22]. The combined impact is that only just a few

vector factors (PCA values) are required to accurately continuously distort the pulmonary. A relevant pulmonary movement phase for one respiratory cycle must be provided for learning purposes to develop a PCA pulmonary dynamic model. In practice, Deformable Image Registration (DIR) among a standard CT stage and most other stages in a 4DCT (or 4DCBCT) information set, which is provided for such therapy model, can be used to do this.

PCA model

After establishing a specified pulmonary movement model so that the modeled image of the rebuilt CT fits very well with the observed x-ray image. However, the intensity values of the calculated and observed beams may be significantly different. We'll presume that they have a direct proportionality here. The functional form is as follows:

$$minimum\ w(j,x,y) = \|Q.t(a,v) - x.a - b - y.1\|_2^2 \quad (3)$$

$$state\ that,\ a = \bar{a} + V.u \quad (4)$$

While a is the specified DVF, 0f is the reference CT, v is the rebuilt CT, f is the prediction image, and Q is a prediction vector that generates the virtual image, and you and are made up of a collection of eigenvalue and PCA coefficients. The period reference has been hidden beneath j, x, and y for simplicity. The technique alternates between the following two stages to find the optimal values for j,x, and y.

Step 1: $j_{m+1} = j_m - \lambda_m.\frac{\partial w}{\partial w_m}$ (5)

Step 2: $(x_{m+1} + y_{m+1})^f - (B^f B)^{-1} B^f Q v_{m+1}$ (6)

Where,

$B = [b,1], and\ \frac{\partial w}{\partial j} = \frac{\partial a}{\partial j}.\frac{\partial b}{\partial a}.\frac{\partial w}{\partial v} = X^f.\frac{\partial v}{\partial a}.Q^f.(Q.v - x.b - y.1).$

Three-dimensional interpolation is used to get the rebuilt CT given the current motion, reduce distortion if m at each cycle. As a result, to find the accurate elevation must be constant with the Interpol method. It comes out is that v/a is a linear function of the image's range observed, scaled by the correct divisor of the DVF, evaluated at the adjacent 8 grid points. Amigos method of linear finding is used to find the scaling factor m in phase 1. The singular device of the objective functions with set w is the version for a bin step 2. As an outcome, the functional form reduces with every phase. It's worth noting that the functional form does have a lower estimate of zero. For all intensive reasons, the interleaved method outlined above could be expected to conform. When the gradient's mean is relatively low or the number of iterations (10 in this work) is achieved, the method ends. We discriminate between two types of DVF to find the accurate carcinoma cell location: press ahead DVF and pull back. (2) Have found a DVF. It can't be used to calculate the freshness lump position directly. To do so, we'll need to have the move forwards inverse. We determine carcinoma position using a fixed-point method for distortion reversal [23].

Filter (Bilateral)

They want to come up with an approach that isn't incremental but achieves the same aims as TVM, namely, reducing local fluctuations (sound, stripes) yet maintaining cohesive local characteristics. A technique like this is the unilateral sieve. It is a quasi filter that combines a range filter and a range sieve for edge-preserving flattening. Two factors, r, and d are necessary when using the Gaussian function to adjust the strength of every strainer. The next contrast, our strainer against a TVM technique to see how well it functions in various situations. The bilateral filter combines the values of comparable and neighboring units in a non-linear manner. Median takes place just inside a specific available space to achieve proper and affective computing. The area classifier and the scope, filter are indeed the 2 different elements.

$$g(a) = \frac{\sum_{t\epsilon M} v(\epsilon)t(\epsilon,a)r(v(\epsilon),v(a))}{\sum_{t\epsilon M} t(\epsilon,a)r(v(\epsilon),v(a))} \quad (7)$$

And a is the geographical parameters, while f is the function. W stands for the input image's window centered at a, while t and r stand for the observed proximity and image pixel matching, accordingly. The physical proximity value seems to be a range screen that controls participation related to spatial distance, whereas the image pixel resemblance value would be a spectrum filter that produces fairly low values for different image pixels. The total of pixel values was forced to 1 after standardization. They utilize Gaussians to simulate the proximity and resemblance measures in our research:

$$t(\epsilon, a) = e^{\frac{|\epsilon - a|}{\rho_\epsilon^3}} \quad (8)$$

$$r(v(\epsilon) = e^{\frac{(v(\epsilon) - v(a)}{\rho_\epsilon^3}} \quad (9)$$

Where ρ_ϵ smoothening control.

The below would be how GPU-accelerated unilateral sorting was performed. The image structure and other parameters were supplied into the GPU, and the drawing destination seems to be a file the length of the source images. By pre-compiling both the near and resemblance functions and preserving them in two 2-dimensional lookup shoulders, they eliminate the costly assessment of the exponential distribution. Bilateral filtering was used in both two and three dimensions

Total variation minimization

The TVM method was also constructed to match it to our unilateral security framework. By reducing the emission level efficiency, the TVM result is found:

$$\text{Minimum } \left\{\frac{|w(a) - v(a)|^2}{2\rho} + \sum_{a=\lambda} |\forall w(a)|\right\} \quad (10)$$

Where, λ is an image, a, v, w, ρ represents spatial input, an input image, solution after sought, and smoothing control respectively. The lateral and vertical variables

in this solution were a and b, correspondingly. The reduction was converted to its double approach, and the regressive project off would be calculated using a quasi steepest descent method.

Proposed work

The quasi reasonable B-spline oriented cardio respiratory phantom had been used to test the system [24]. These computational apparitions were anatomically accurate to a considerable degree. The breathing, the movement was created using fundamental breathing mechanical understanding. As our simulated 4DCT, they made an effective NCAT spectrum with ten stages. The 3D lump location, which is employed as actual data, is also generated by the NCAT spectra. DIR between the finish to expiration phase and most other stages, using the finish to expiration stage as the reference image. The DIR method is a GPU-based quick demonic method [25]. The 9 DVF from DIR were then Principal Component Analysis, with 3 PCA correlations and support vectors maintained in this method. Applying Siddon's method [26], we generated x-ray images at various stages to those used for learning, with varying respiration frequency and amplitude and crane directions. There were no embedded calibration devices on this client, thus true 3D lump localization was not accessible to assess our approach. Rather, the projection of the predicted 3D lump area onto a 2D imaging system and matched it to what a doctor had manually defined. The lump center point was determined for every projector from the physician outline and utilized as the actual truth to test the method. The lump location error was found in both axis and futures, and both were scaled down to the average lump location.

Results and Discussions

They put their system's extension ability to the test by launching a unique CT space with a 50% rise in respiratory frequency significance (16 mm in learning rather than 24 mm in assessment). The generated forecast image (sees Figure 1) was created at the end of the breathing period to be as dissimilar from the standard CT as possible. During 10 rounds, the efficient approaches. The standard CT's axial and frontal views, and the variation images, are shown in Figure 2. The initial relative 3D RMS image rebuilt error is 35%, and it resembles that produced by 3D DIR plus demonic.

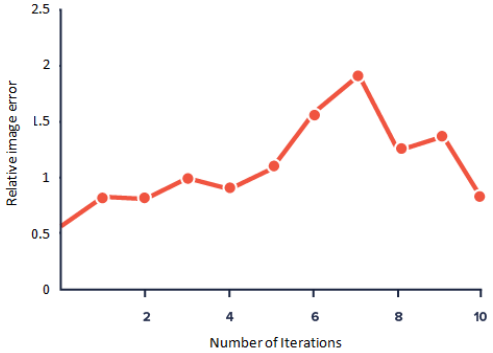

Figure 1. Number of iterations Vs Relative Image Error

Image 1: a) "calculated" extrapolation for the sample image at an RPO direction; b) performance depends (top) and comparison image rebuilt mistake (under) at every repetition. They next performed a somewhat more thorough analysis by developing an interactive specter with 60 phases, a 50% rise in respiratory intensity, and a 4-sec time. They created 360 presentations in 1 minute by simulating conical flare x-ray images throughout all directions with a 1° gap (15 breathing cycles). Comparative 3D image rebuilt mistake is 7.5 percent, 2.4 percent of median. The typical 3D carcinoma location mistake is 0.9 mm, 0.5 mm, and presentation directions have little effect Figure 3. Our approach was built over an NVIDIA C1060 GPU to quicken up the processing. To reduce the computational effort, even more, we re-used the PCA characteristics from the before image. To every prediction, the image rebuilt and carcinoma location took between 0.2 and 0.3 seconds.

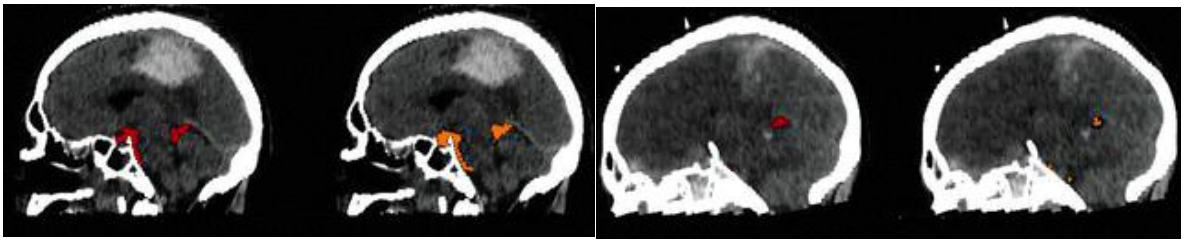

Figure 2. Sagittal view of the human brain of test CT and reference CT

Image 2: Midline aspect shows a variety of images between a) assessment and standard CT; b) test CT and CT rebuilt with an optimization technique. Upper row: comparative image defect like a product of multislice angular position between the dataset test image for normal respiration and: standard image (dashed line); image rebuilt using the proposed technique (solid line). Under row: identical to upper row, except a 3D location issue. Approximately 650 images were recorded for such a subject throughout an entire crane revolution at a speed of around 10.7 Hz. The carcinoma is only apparent in a subset of these images because the stereotactic scanning was conducted in ½ configurations. The physician marked the carcinoma in the longest continuous set of images in which it was apparent. 281 predictions were used in this case.

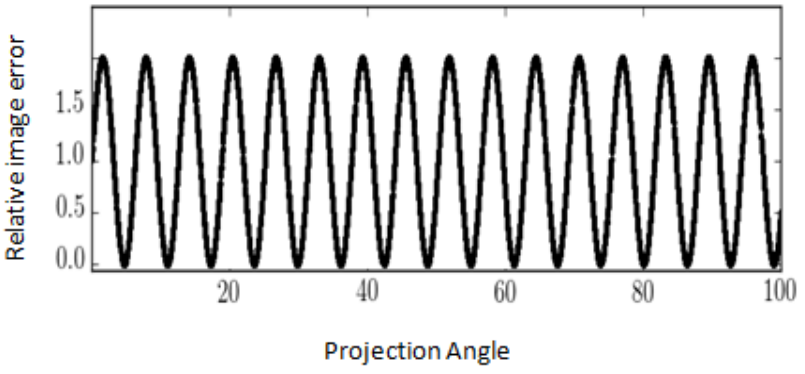

Figure 3. Relative Image Error Vs Projection angle

The following figure shows the client's carcinoma location outcomes. The lines reflect the physician carcinoma location, whereas the pixels indicate the system outcome. During the CBCT scan, the client's respiration was highly erratic, for both foundation deviation and intensity alterations. The carcinoma location outcomes are seen in Figure 4. The average localization mistake in the longitudinal axis is 1.9 x 0.9 mm. The median inaccuracy in the perpendicular direction is 1.8x1.0 mm. On an NVIDIA Tesla C1060 GPU card, the median calculation time for image rebuilt and carcinoma location from every projection was roughly 0.3 seconds.

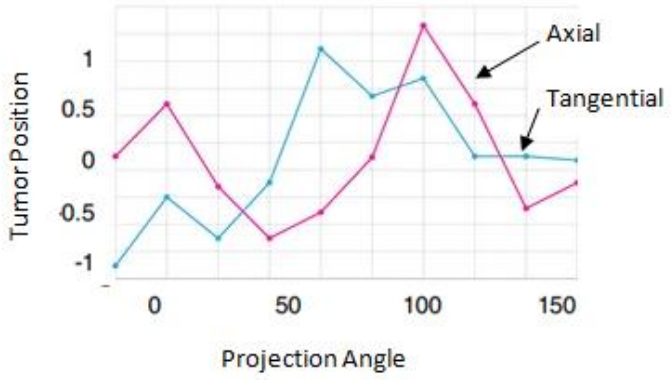

Figure 4. Tumor localization between Axial and Tangential tumor position Vs Projection angle

Our testing was performed on a GLSL-programmed NVIDIA GTX 280 GPU and an Intel Core 2 Quad CPU operates at 2.66GHz and 2.67GHz. Our findings were divided into two categories: (1) the OS-SIRT findings, which show the link between sound levels and parameterization; and (2) the efficiency of GPU-accelerated filter bank, which uses Cg and CUDA, and the rebuilding outcomes utilizing unilateral strainer and overall variation reduction. The effectiveness of the alternative rebuilding approaches was assessed using the 2-dimensional Infant Brain training sample (size 2562). In similar image seeing patterns, produced 180 images with the uniform angular spacing of [-90, +90]. The forecast information was then subjected to various amounts of Gaussian noise, yielding SNRs of 15, 10, 5, and 1. Figure 5 gives the overall rebuilding outcomes for every SNR at the shortest ceiling clock period (using the coefficient of correlation CC between the actual and rebuilt image).

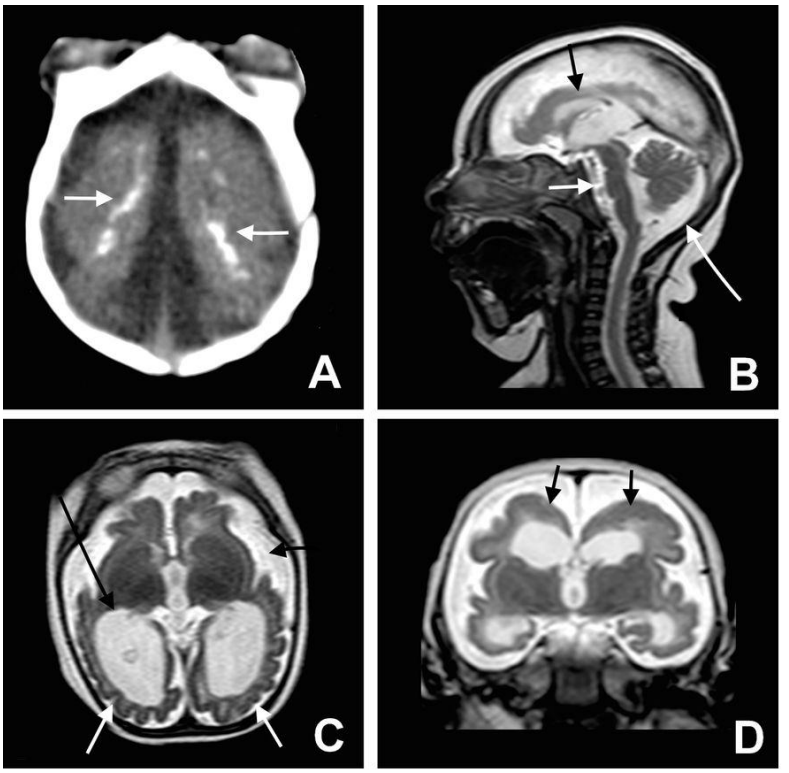

Figure 5. Reconstructions of the head test image produced with various SNR levels (a) Original (b) Noise-free (c) SNR 5 (d) SNR 10

The predicted optimal settings discovered through rigorous real-world tests are very dependent on the specific image matter at hand, including such SNR, the overall number of forecasts and its geographical scope, imaged item, machine, and so on. The effect of SNR is depicted in Figure 6. For every projected SNR value, the figure provides quantifiable advice on how to choose the greatest amount of subgroups and the related (to acquire the greatest possible quality in the shortest time). Low SNR, for instance, necessitates a small number of subgroups in the rebuilding process to gain extra flattening. The stress relief ratio was proportional to either the subgroup amount and the sound intensity. The arc of that is essentially a small bit continuous for every sound level, with such a pivotal moment at a certain subgroup amount. In illustrating, during subgroup no.1 to 60, the ratings for SNR 10 are 1, then reduce until reaching the minimum number of 0.4 subgroup amount 180. It is a significant difference from the generalized linear employed on [118] – a greeter would lead to quicker resolution, and as our extensive standard studies have shown, it will also produce much more accurate findings.

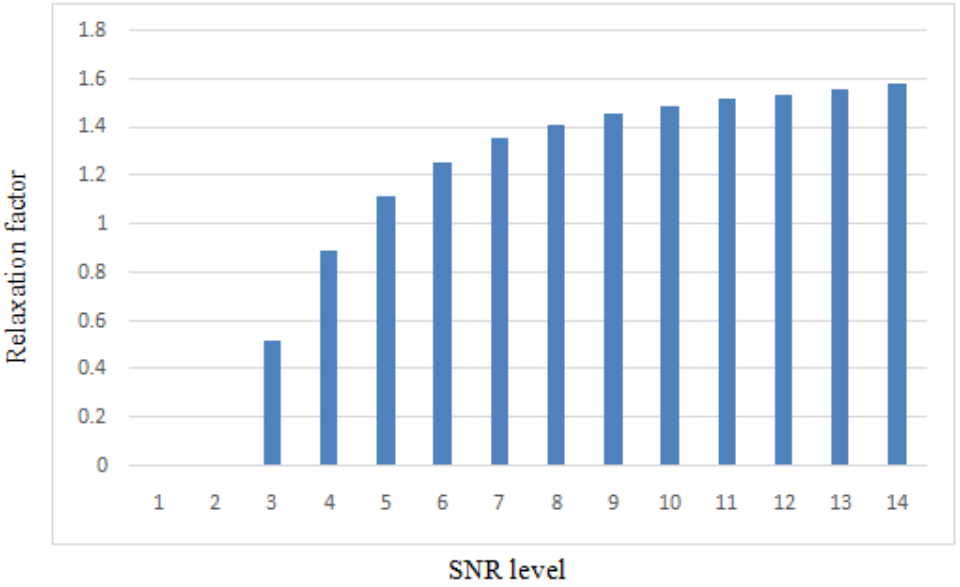

Figure 6. Graph between SNR and Relaxation Factor

Table 1
Comparison between CPU bilateral filter and GPU's Clock Time

Test Size	Size of Window	Time (CPU)	Time (GPU)	Time (CUDA)
256 x 256	9 x 9	0.8	0.008	0.006
512 x512	9 x 9	3.06	0.013	0.008
1024 x 1024	15 x 15	12.72	0.025	0.019
256 x 256 x 256	15 x 15 x 15	>500	5.639	Not Applicable

Across both CPU and GPU, examined the accuracy of both 2 dimensional and 3-dimensional bilateral effects with various image and window sizes (using Cg). Table 1 indicates that using the GPU could bring intake great interest of much more than a factor of two. It also created a CUDA implementation of our technique for 2-dimensional images.

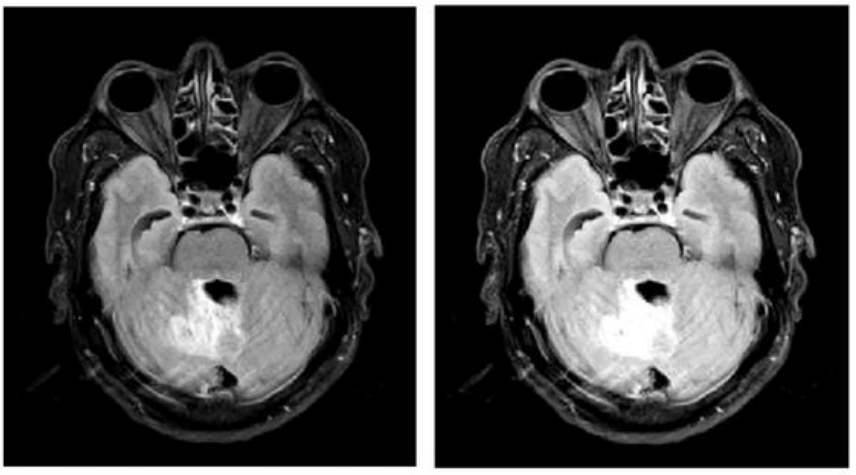

Figure 7. Comparison between the case of noise-free and few-view

They have been using the NIH Visual Person collection using 512x3 resolution to measure the validity of such normalized rebuilding both in the few views and loud (SNR=10) scenarios. For the sound only in several cases, they utilized SART using 8 repetitions. The shape of the intensity range was set to 11. Figure 7 depicts a layer of the rebuilt area, both with sifting across rebuilt from 90, 60, and 30 views, correspondingly. SART has been well adapted just for a few rebuilding, as we can see. Studied a range of pairings of typical r and d for the normalized rebuild and chose the great outcomes. The 30-view rebuild, especially, exhibits strong streaks artifacts that could be eliminated by interim unilateral lens normalization. For the Visual Person collected at 512x3 resolutions for both 180 and 30 forecasts, Figure 8 shows the GPU-accelerated rebuilding amount of time needed with one SART repetition. The 1-ch period just utilizes the GPU equipment's R-channel, whereas the 4-ch period employs every four (RGBA) streams simultaneously. Normalization through filtering methods adds just a minor time, cost, whereas using four ports offers a 2.5-fold speed boost. Notice that they selected SART as the worst method to demonstrate the OS-SIRT family's period performance's lower limit.

Table 2
Time for one GPU-acceleration SART interaction

P	1 Ch	1 Ch w/bf	4 Ch	4 Ch w/bf
360	92	96	35	35
60	23	26	10	12

A comparative approach

Figure 8 displays the effects of evaluating so same layer with similar parameters for both, the only several (30 forecasts) and loud only several (30 forecasts and SNR=10) instances. They find that unilateral processing provides comparable findings to TVM within the sound situation (maybe even slightly better). In the load scenario, although, the TVM is preferable. It wasn't unexpected, given that

TVM sets a limit on the image, but unilateral screening simply means surrounding data, but remove the entire sound at greater sound levels. Most, meanwhile, effectively retain essential components while eliminating sound and streaked distortions.

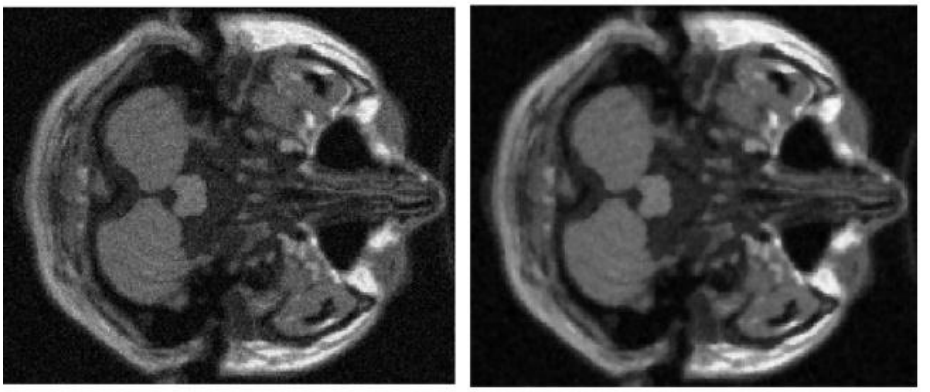

Figure 8. Comparison between bilateral filtering and TVM

Conclusions

In literally seconds, we were able to recover pulmonary movement data from a single x-ray image. To allow faster calculation, even more, we can use earlier records to anticipate the present PCA coefficients or use it as a beginning point. We intend to test the system's effectiveness on a larger variety of healthcare information. That's important to note the stronger DIR methods and diligent product testing would assist enhance the system's reliability for client records. It's also unclear whether the PCA motion prototype will be capable of capturing significant differences in respiratory rates between treatment trials and treatment portions. If this happens, a 4D CBCT taken on the day of therapy may be a better choice for creating the PCA dynamic technique.

References

[1] Giraud P, Antoine M, Larrouy A, Milleron B, Callard P, De Rycke Y, Carette MF, Rosenwald JC, Cosset JM, Housset M, Touboul E. Evaluation of microscopic tumor extension in non–small-cell lung cancer for three-dimensional conformal radiotherapy planning. International Journal of Radiation Oncology* Biology* Physics. 2000 Nov 1;48(4):1015-24.

[2] Karnan, B., Kuppusamy, A., Latchoumi, T. P., Banerjee, A., Sinha, A., Biswas, A., & Subramanian, A. K. (2022). Multi-response Optimization of Turning Parameters for Cryogenically Treated and Tempered WC–Co Inserts. Journal of The Institution of Engineers (India): Series D, 1-12.

[3] Aroulanandam, V. V., Latchoumi, T. P., Bhavya, B., & Sultana, S. S. (2019). Object detection in convolution neural networks using iterative refinements. architecture, 15, 17.

[4] Latchoumi, T. P., Reddy, M. S., & Balamurugan, K. (2020). Applied Machine Learning Predictive Analytics to SQL Injection Attack Detection and Prevention. European Journal of Molecular & Clinical Medicine, 7(02), 2020.

[5] Banu, J. F., Muneeshwari, P., Raja, K., Suresh, S., Latchoumi, T. P., & Deepan, S. (2022, January). Ontology Based Image Retrieval by Utilizing Model Annotations and Content. In *2022 12th International Conference on Cloud Computing, Data Science & Engineering (Confluence)* (pp. 300-305). IEEE.

[6] Karnan, B., Kuppusamy, A., Latchoumi, T. P., Banerjee, A., Sinha, A., Biswas, A., & Subramanian, A. K. (2022). Multi-response Optimization of Turning Parameters for Cryogenically Treated and Tempered WC–Co Inserts. Journal of The Institution of Engineers (India): Series D, 1-12.

[7] Garikapati, P., Balamurugan, K., Latchoumi, T. P., &Malkapuram, R. (2021). A Cluster-Profile Comparative Study on Machining AlSi 7/63% of SiC Hybrid Composite Using Agglomerative Hierarchical Clustering and K-Means. Silicon, 13, 961-972.

[8] Romaguera LV, Mezheritsky T, Mansour R, Tanguay W, Kadoury S. Predictive online 3D target tracking with population-based generative networks for image-guided radiotherapy. International Journal of Computer Assisted Radiology and Surgery. 2021 Jun 10:1-3.

[9] Garikapati, P. R., Balamurugan, K., Latchoumi, T. P., & Shankar, G. (2022). A Quantitative Study of Small Dataset Machining by Agglomerative Hierarchical Cluster and K-Medoid. In Emergent Converging Technologies and Biomedical Systems (pp. 717-727). Springer, Singapore.

[10] Dr.P.Sivakumar, “Design and analysis the performance of real time content delivery network using beam scanning” journal of critical reviews, ISSN-2394-5125 VOL 7, ISSUE 04, 2020.

[11] Ezhilarasi, T. P., Dilip, G., Latchoumi, T. P., & Balamurugan, K. (2020). UIP—A Smart Web Application to Manage Network Environments. In Proceedings of the Third International Conference on Computational Intelligence and Informatics (pp. 97-108). Springer, Singapore.

[12] Xue P, Fu Y, Ji H, Cui W, Dong E. Lung Respiratory Motion Estimation Based on Fast Kalman Filtering and 4D CT Image Registration. IEEE Journal of Biomedical and Health Informatics. 2020 Oct 12.

[13] Latchoumi, T. P., Balamurugan, K., Dinesh, K., &Ezhilarasi, T. P. (2019). Particle swarm optimization approach for waterjet cavitation peening. Measurement, 141, 184-189.

[14] Krieger M, Giger A, Salomir R, Bieri O, Celicanin Z, Cattin PC, Lomax AJ, Weber DC, Zhang Y. Impact of internal target volume definition for pencil beam scanned proton treatment planning in the presence of respiratory motion variability for lung cancer: A proof of concept. Radiotherapy and oncology. 2020 Apr 1;145:154-61.

[15] Ting LL, Chuang HC, Liao AH, Kuo CC, Yu HW, Tsai HC, Tien DC, Jeng SC, Chiou JF. Tumor motion tracking based on a four-dimensional computed tomography respiratory motion model driven by an ultrasound tracking technique. Quantitative imaging in medicine and surgery. 2020 Jan;10(1):26.

[16] Iwasawa T. Principles and Clinical Applications of Respiratory Motion Assessment Using 4D Computed Tomography and Magnetic Resonance Imaging. In Pulmonary Functional Imaging 2021 (pp. 91-106). Springer, Cham.

[17] Latchoumi, T. P., Kalusuraman, G., Banu, J. F., Yookesh, T. L., Ezhilarasi, T. P., & Balamurugan, K. (2021, November). Enhancement in manufacturing systems using Grey-Fuzzy and LK-SVM approach. In 2021 IEEE International

Conference on Intelligent Systems, Smart and Green Technologies (ICISSGT) (pp. 72-78). IEEE.
[18] Romaguera LV, Plantefève R, Romero FP, Hébert F, Carrier JF, Kadoury S. Prediction of in-plane organ deformation during free-breathing radiotherapy via discriminative spatial transformer networks. Medical image analysis. 2020 Aug 1;64:101754.
[19] Xu F, Xu W, Jones M, Keszthelyi B, Sedat J, Agard D, Mueller K. On the efficiency of iterative ordered subset reconstruction algorithms for acceleration on GPUs. Computer methods and programs in biomedicine. 2010 Jun 1;98(3):261-70.
[20] Gregor J, Benson T. Computational analysis and improvement of SIRT. IEEE transactions on medical imaging. 2008 Jun 24;27(7):918-24.
[21] Mattern, Shannon. *Code and clay, data and dirt: Five thousand years of urban media*. U of Minnesota Press, 2017.
[22] Acemoglu, Daron, et al. *A multi-risk SIR model with optimally targeted lockdown*. Vol. 2020. Cambridge, MA: National Bureau of Economic Research, 2020.
[23] Ricke, Jens, et al. "Impact of combined selective internal radiation therapy and sorafenib on survival in advanced hepatocellular carcinoma." *Journal of hepatology* 71.6 (2019): 1164-1174.
[24] Liu, Yang, Chuanjiang He, and Yongfei Wu. "Variational model with kernel metric-based data term for noisy image segmentation." *Digital Signal Processing* 78 (2018): 42-55.
[25] Liang, Jiuzhen, Min Li, and Cuicui Liao. "Efficient numerical schemes for Chan-Vese active contour models in image segmentation." *Multimedia Tools and Applications* 77.13 (2018): 16661-16684.
[26] Dellmann MF, Jerg KI, Stratemeier J, Heiman R, Hesser JW, Aschenbrenner KP, Blessing M. Noise-robust breathing-phase estimation on marker-free, ultra low dose X-ray projections for real-time tumor localization via surrogate structures. Zeitschrift für Medizinische Physik. 2021 Jun 2.
[27] Alina G, Krieger M, Jud C, Duetschler A, Salomir R, Bieri O, Bauman G, Nguyen D, Weber DC, Lomax AJ, Zhang Y. Liver-ultrasound based motion modelling to estimate 4D dose distributions for lung tumours in scanned proton therapy. Physics in Medicine & Biology. 2020 Dec 21;65(23):235050.
[28] Sakly H, Mourad SA, Radhouane S, Tagina M. Medical decision making for 5D cardiac model: template matching technique and simulation of the fifth dimension. Computer methods and programs in biomedicine. 2020 Jul 1;191:105382.
[29] Willett FR, Deo DR, Avansino DT, Rezaii P, Hochberg LR, Henderson JM, Shenoy KV. Hand knob area of premotor cortex represents the whole body in a compositional way. Cell. 2020 Apr 16;181(2):396-409.
[30] Cai J, Wang Y, Liu A, McKeown MJ, Wang ZJ. Novel regional activity representation with constrained canonical correlation analysis for brain connectivity network estimation. IEEE transactions on medical imaging. 2020 Jan 30;39(7):2363-73.
[31] Chang Y, Jiang Z, Segars WP, Zhang Z, Lafata K, Cai J, Yin FF, Ren L. A generative adversarial network (GAN)-based technique for synthesizing realistic respiratory motion in the extended cardiac-torso (XCAT) phantoms. Physics in Medicine & Biology. 2021 May 31;66(11):115018.